AIAA JOURNAL
Vol. 47, No. 11, November 2009

Effect of Rotation Kinematics and Angle of Attack on Flapping Flight

Pradeep Gopalakrishnan* and Danesh K. Tafti†
Virginia Polytechnic Institute and State University, Blacksburg, Virginia 24061

DOI: 10.2514/1.37540

Unsteady aerodynamics of a rigid flapping wing at a Reynolds number of 10,000 for forward flight with an advance ratio of 0.5 is analyzed. A spiral leading-edge vortex with a strong spanwise flow along its core is formed during the downstroke, resulting in a peak lift and thrust. A negative spanwise flow formed due to the tip vortex prevents the removal of vorticity from the leading-edge vortex, leading to instability and separation of the leading-edge vortex. Analysis of different rotation timings shows that supination results in the leading-edge vortex formation near the base and its strength depends on the flapping velocity. A stronger vortex is formed for advanced rotation and it generates high lift. Delayed rotation affects thrust production during translation and results in low propulsive efficiency. Analysis of rotation duration shows that shorter rotation results in high instantaneous lift values, whereas continuous long-duration rotation results in high thrust and propulsive efficiency. Analysis of different angles of attack show that a moderate angle of attack, which results in a high thrust-to-lift ratio and complete shedding of the leading-edge vortex at the end of translation, is required for high propulsive efficiency.

Nomenclature

$\mathbf{a}^i$	=	contravariant basis vectors
C	=	midspan chord length
C_L	=	coefficient of lift
C_T	=	coefficient of thrust
F	=	force acting on the wing
f	=	frequency of flapping
$\sqrt{g}$	=	Jacobian of the transformation
g^{ij}	=	contravariant metric tensor
$\sqrt{g}U^j$	=	contravariant flux vector
$\sqrt{g}U_g^j$	=	contravariant flux due to grid movement
J	=	advance ratio (U_∞/U_f), ratio of the flight velocity to the flapping velocity
P	=	power
p	=	pressure
R	=	semiwingspan
Re	=	Reynolds number ($U_f c/\nu$)
Re_t	=	inverse of the turbulent viscosity
Uf	=	flapping velocity; $2\Phi f R$
U_∞	=	freestream velocity, forward-flight velocity
u_i	=	Cartesian velocity vector
u_i^g	=	Cartesian grid velocity vector
$\mathbf{x}$	=	physical space coordinate
α	=	angle of attack
β	=	stroke plane angle
η_{prop}	=	propulsive efficiency
ν	=	kinematic viscosity
$\boldsymbol{\xi}$	=	computational space coordinate
ρ	=	torsional angle
τ	=	shear stress on the surface of the wing
Φ	=	total flapping amplitude (maximum to minimum)
ϕ	=	flapping amplitude
Ω	=	angular velocity
ω	=	vorticity

Subscripts

d	=	downstroke
eff	=	effective
u	=	upstroke
x, y, z	=	fixed reference frame
ξ, η, ζ	=	rotating reference frame

Received 14 March 2008; revision received 22 December 2008; accepted for publication 2 February 2009.

*Graduate Student, Mechanical Engineering, 114K, Randolph Hall. Student Member AIAA.

†Professor, Mechanical Engineering, 114I, Randolph Hall. Member AIAA.

I. Introduction

MICRO air vehicles (MAVs) typically have dimensions of less than 15–20 cm with gross takeoff weights of around 100 to 200 g and flight speeds of around 10–15 m/s, which corresponds to a Reynolds number range between 10,000 and 100,000. At these low Reynolds numbers, the aerodynamic efficiency (lift-to-drag ratio) of conventional fixed airfoils rapidly deteriorates [1]. The chief reason for the deterioration in performance is that at low Reynolds numbers, the boundary layer remains laminar downstream of the location of minimum pressure on the airfoil, making it very susceptible to flow separation as the angle of attack increases, resulting in an early onset of stall (Carmichael [2]). In addition, because of the low-aspect-ratio wings used in MAVs, the tip vortex covers a major part of the wing and the aerodynamic performance is greatly affected by the shedding of the tip vortices (Pelletier and Mueller [3]). On the other hand, birds and insects for which the flight regime coincides with that of MAVs use flapping wings to provide both lift and thrust efficiently. They do this by taking advantage of unsteady flow mechanisms using wing kinematics evolved over millions of years. The kinematics involved in normal flapping flight are divided into two translation motions corresponding to up- and downstrokes and two rotational motions (pronation and supination) corresponding to stroke reversals. Pronation is achieved before the downstroke and supination is achieved before the upstroke. Figure 1 shows the critical kinematic parameters of flapping flight, with their definitions given in Table. 1.

A number of unsteady aerodynamic mechanisms such as clap and fling [4], delayed stall [5,6], wake capturing [7], and rotational circulation [7] have been proposed to explain the generation of lift in birds and insects. Among these, the delayed-stall mechanism involves the formation of a stable leading-edge vortex (LEV) and is the primary mechanism used by most birds and insects for production of lift and thrust during the translational period. During the downstroke, air swirls around the leading edge and forms a LEV. This LEV increases the bound vortex circulation and hence the lift. In a fixed airfoil, the formation of the LEV leads to dynamic stall within

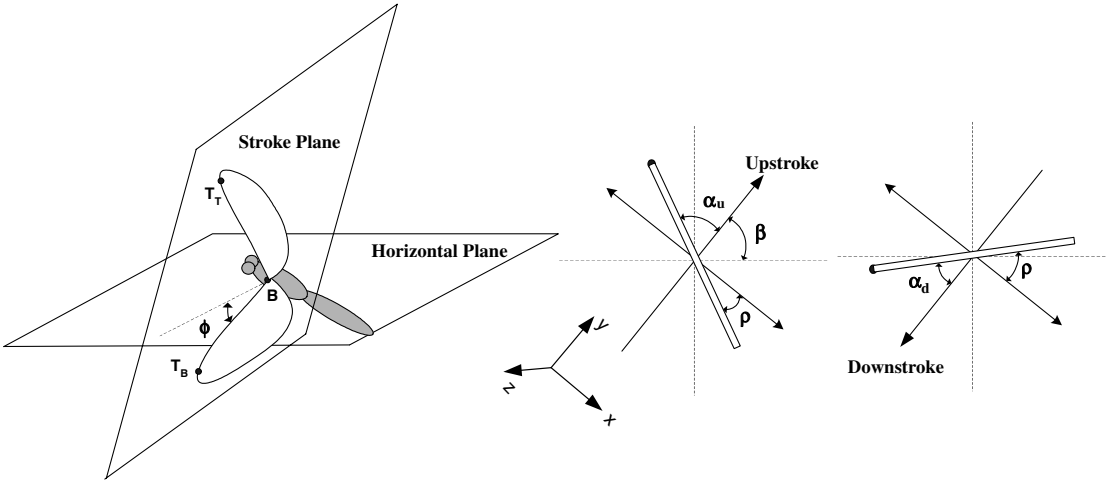

Fig. 1 Kinematic parameters.

three–four chord lengths of travel. However, in insects, the LEV is stable for the entire downstroke, and during this period the insect covers a distance of more than eight chord lengths.

The stability of the LEV plays an important role in the superior performance of birds and insects. Many experimental studies have evaluated the duration and stability criteria of the LEV. Dickinson and Götz [5] analyzed the effect of angle of attack during the translation period on lift and drag production using a two-dimensional-wing model ($Re = 192$). They found that the LEV was generated at an angle of attack above 13.5 deg, due to impulsive movement, and stayed attached for two chord lengths of travel. The presence of the LEV resulted in an 80% increase in lift, similar to that of detached vortex lift for a delta-wing aircraft. The shedding of the LEV led to the formation of a secondary vortex of opposite sign near the trailing edge, correlating with a decrease in lift. Further, the study found that up to an angle of attack of 54 deg, the lift characteristics remain unaltered by the change in camber. Wang et al. [8] compared results obtained from two-dimensional numerical simulation of a hovering fruit fly with three-dimensional results from a dynamically scaled mechanical model ($Re = 75$ to 115). They found that the numerical results matched well with three-dimensional results for cases with a short downstroke length. In the case of hovering insects, the stroke length is only three to five chords, during which the LEV remains attached to the wing even for two-dimensional cases. When the downstroke is longer than a typical stroke length, the two-dimensional cases showed a phase difference with three-dimensional results and resulted in lower lift coefficients.

Ellington [9] conducted flow-visualization studies using a large mechanical model of a hawk moth, *flapper* ($Re \sim 4000$). An intense LEV on the downstroke at all flight speeds (0.4 to 5.7 m/s) was observed. The LEV spiraled out toward the wingtip with high spanwise velocities comparable with the flapping velocity, which stabilized the vortex. The flow structure obtained was similar to the conical leading-edge vortex found in delta wings. He suggested that the strong spanwise flow was created either by the pressure gradient, formed due to the velocity gradient along the flapping wing, or by centrifugal acceleration in the boundary layer, or by the induced velocity field of the spiral vortex lines. Liu et al. [10] analyzed the flapping flight of a hovering hawk moth at $Re = 3000$ to 4000 using the finite volume method. The study showed the formation of a LEV during both upstroke and downstroke, which stayed attached to the wing during the entire translational and following rotational motions. The combined translation and rotation deformed the vortex, which led to shedding of the LEV at the start of the next translation motion. The spanwise flow, created due to spanwise pressure gradient, stabilized the LEV until 70% of the span. During the second half of the downstroke, a secondary LEV formed at 75% span, which was unstable and strongly affected by the presence of the tip vortex. The LEV formed during the upstroke was weak and closely attached to the leading edge. The study showed that the lift force was produced mainly during the entire downstroke and the later part of the upstroke.

Dickinson et al. [7] conducted flow-visualization studies using a dynamically scaled version of a hovering fruit fly, *robotic fly*, at $Re = 136$. They compared the force coefficients obtained by the robotic fly with a two-dimensional model wing and found that the 3-D model produced high average lift and thrust coefficients. The experimental investigation of Birch and Dickinson [11] provided contrasting proof for the stability of the LEV at low Reynolds numbers (100–250) relevant to small insect flights. They conducted experiments with fences and baffles on the top surface of the wing and showed that the LEV remains attached to the wing despite the absence of spanwise flow. They proposed that the downward velocity created by the tip vortices limited the growth and subsequent detachment of the LEV. Birch et al. [12] investigated flow structures and forces generated at low and high Reynolds numbers ($Re = 120$ and 1400). In both cases, a stable LEV was present throughout the downstroke. At $Re = 1400$, they observed strong spanwise flow within the core of the LEV, with velocities of 150% of that of the flapping velocity. The spanwise flow removed the vorticity into the wake and resulted in a spiral LEV similar to that observed by Ellington [9]. However, at $Re = 120$, the spanwise flow was absent, which resulted in lower forces. Miller and Peskin [13] studied the effect of Reynolds numbers (8 to 128) on the formation of the LEV using the immersed-boundary technique. At $Re < 32$, the LEV (negative-pressure region) and trailing-edge vortices (positive-pressure region) remain attached, which resulted in lower lift. At $Re < 64$, they observed shedding of the trailing vortex during

Table 1 Kinematic parameters and nondimensional numbers for flapping flight

Parameters	Description
Stroke plane	The plane defined by three points: wing base B, wingtip at maximum T_T, and minimum angular position T_B. During hovering the stroke plane will be near horizontal, and during forward flight it will be vertical.
Stroke plane angle β	Angle between the stroke plane and the horizontal plane. It ranges from 0 deg for hovering to 90 deg for forward flight.
Angle of attack α	Angle between the wing direction (from trailing edge to leading edge) and the direction of motion.
Torsional angle ρ	Angle between the wing direction and the direction perpendicular to the stroke plane.
Flapping amplitude ϕ	Angle between the leading edge of the wing and the plane perpendicular to the stroke plane.

translation, which resulted in vortical asymmetry, leading to high lift production.

Shyy and Liu [14] carried out a computational fluid dynamics (CFD) analysis of a fruit fly ($Re = 120$) and a hawk moth ($Re=$ 6000) using wing–body models. For the fruit fly, they observed a stable LEV connected with the tip vortex throughout the translation, whereas for the hawk moth, the vortex breaks down approximately at three-quarters of the span toward the tip. They also observed the presence of a strong spanwise flow for the hawk moth, whereas it was only 2–5% of the average tip velocity for the fruit fly. The CFD analysis of Aono et al. [15] with an actual wing–body hawk moth model observed a horseshoe-shaped vortex [combined LEV, tip vortex, and trailing-edge vortex (TEV)] during the middle of the down- and upstrokes that subsequently grew into a doughnut-shaped vortex near the end of translation. The critical observation in their study was the interaction of the shed TEV with the body, which led to the formation of the doughnut-shaped vortex ring. A similar looplike vortex structure was reported by McClung et al. [16] and by Ramamurti and Sandberg [17,18], who analyzed hovering and maneuvering flight of a fruit fly with the actual wing kinematics captured by Fry et al. [19]. They computed the yaw moment and concluded that thrust force and a component of lift force combine to produce the turning moment required for maneuvering and that the side force alone produces the restoring torque. The experiments of Fry et al. [19] using a mechanical model of a fruit fly showed that subtle changes in the phasing of the stroke angle and the stroke deviation angle between the left and right wings produced sufficient torque required for maneuvering.

Tarascio et al. [20] conducted a flow-visualization experiment on a hovering flapping flight model at a Reynolds number on the order of 8000. The flowfield consisted of folded wakes formed by the strong starting vortex shed at the end of each half-stroke during wing rotation. Because of the induced flow, the wakes were pushed downward, parallel to the flapping plane. The key finding of this study was that during translation, the top surface was covered by multiple vortices and the LEV was continually generated and shed into the wake. This result is in contrast to previous studies [7,9], in which a stable single LEV is present during translation. Further, they observed that the strength of the LEV increased along the span and identified separated flow at the outboard region of the wing.

The unsteady mechanisms involved during stroke reversal contributed significantly to lift production, especially for hovering flight. In the experimental study by Dickinson et al. [7], two peaks in force coefficients were obtained during the rotation and early part of translation. They attributed the peak in lift during the rotation to the rotational circulation and the second peak to wake capturing. Dickinson [21] studied the effect of rotation by varying speed, duration, angle of attack, and axis of rotation using a dynamically scaled model ($Re = 236$) of small insects (*Drosophila*) during hovering. The study showed that the aerodynamic performance increased significantly as the wing captured the vorticity generated during rotation. A lift-coefficient value of 4 was obtained when the wing translated backward in the von Kármán street generated by the previous stroke with a 76.5 deg angle of attack. Effects of stroke amplitude, rotation timing and duration, and shape and magnitude of stroke deviation on the aerodynamic performance was studied by Sane and Dickinson [22] using a robotic fly. The values of drag showed large deviations from translational quasi-steady values at low stroke amplitudes due to the major influence of rotational mechanisms. Analysis on timing and duration of rotation showed that the short rotation, which precedes the translation (occurring at the end of the stroke), resulted in high lift. Further, they found that the quasi-steady analysis underestimated the average thrust coefficient in all cases, showing the importance of unsteady aerodynamics.

A numerical investigation of a hovering fruit fly by Sun and Tang [23] with rotation timing similar to that of Sane and Dickinson [22] showed a comparable trend in lift and thrust. However, their results showed that wake capturing and rotational circulation effects are not significant and they proposed three other mechanisms: fast acceleration at the start of downstroke, delayed stall during translation, and fast pitching-up rotation at the end of the stroke for force production. When the rotation or stroke reversal was carried out at the end of the stroke, the effect of the first and third mechanisms were enhanced, which resulted in high lift. When the rotation was symmetric (half of the rotation during the end of the stroke and half during the start of the following stroke), the fast acceleration mechanism at the start of the stroke was affected, resulting in lower lift. The performance deteriorated when rotation occurred at the start of the stroke, which completely eliminated the pitching-up rotation mechanism. Ramamurti and Sandberg [24] also showed that the thrust force was high when rotation was advanced with respect to stroke reversal.

Despite many available studies, application of flapping flights to MAVs still pose a number of challenges. Most of the previous studies have been performed at very low Reynolds numbers, less than 4000, whereas MAVs could have an operational range extending to between 10,000 and 100,000. Further, the experiments by Tarascio et al. [20] at $Re = 8000$ show the presence of multiple unstable vortices on the top surface of the wing, which is in contrast to the stable LEV formation during the delayed stall. This necessitates more detailed studies to evaluate the effectiveness of delayed stall in a high Reynolds number range relevant to MAVs. Flow-visualization [25] studies show that insects employ different kinematics at different flight conditions to achieve the required thrust. However, most of the previous studies have concentrated on hovering flight, which requires no thrust. Hence, it is critical to understand how changes in kinematics affect thrust production for forward flight. The focus of the present study is to analyze the effect of kinematics on forward flight with an advance ratio $J = 0.5$ at $Re = 10,000$. The simulations are carried out for different kinematics by varying rotation timing, rotation duration, and angle of attack. The effects of kinematics are evaluated by analyzing the resulting flow structure, force production, and propulsive efficiency.

II. Methodology

A. Governing Equations

In the present study, a structured multiblock solver with a boundary-fitted dynamic grid is employed. In this framework, the grid deforms with the wing motion. The method of large eddy simulation is employed with a subgrid stress model to resolve the turbulence in the flowfield. The governing equations for unsteady incompressible viscous flow on a moving coordinate system consist of space, mass, and momentum conservation laws. The equations are mapped from physical $\mathbf{x}$ to logical/computational space $\boldsymbol{\xi}$ by a boundary-conforming transformation $\mathbf{x} = \mathbf{x}(\boldsymbol{\xi})$, where $\mathbf{x} = (x, y, z)$ and $\boldsymbol{\xi} = (\xi, \eta, \zeta)$. The equations are nondimensionalized by chord length C and flapping velocity U_f and are written in conservative nondimensional form as follows.

Space:

$$\frac{\partial}{\partial t}(\sqrt{g}) - \frac{\partial}{\partial \xi_j}(\sqrt{g}U_g^j) = 0 \tag{1}$$

Mass:

$$\frac{\partial}{\partial \xi_j}(\sqrt{g}U^j) = 0 \tag{2}$$

Momentum:

$$\frac{\partial}{\partial t}(\sqrt{g}u_i) + \frac{\partial}{\partial \xi_j}([\sqrt{g}U^j - \sqrt{g}U_g^j]u_i) = -\frac{\partial}{\partial \xi_j}(\sqrt{g}(\mathbf{a}^j)_i p) + \frac{\partial}{\partial \xi_j}\left(\left(\frac{1}{Re} + \frac{1}{Re_t}\right)\sqrt{g}g^{jk}\frac{\partial u_i}{\partial \xi_k}\right) \tag{3}$$

where $\mathbf{a}^i$ are the contravariant basis vectors, $\sqrt{g}$ is the Jacobian of the transformation, g^{ij} is the contravariant metric tensor, $\sqrt{g}U^j = \sqrt{g}(\mathbf{a}^j)_k u_k$ is the contravariant flux vector, $\sqrt{g}U_g^j = \sqrt{g}(\mathbf{a}^j)_k u_k^g$ is the contravariant flux vector due to grid velocity u^g, u_i is the Cartesian velocity vector, and p is the pressure. In the preceding formulation, the grid velocity u^g is not computed explicitly. Instead,

the grid contravariant flux vector is employed, which is directly computed based on the space conservation law [26,27]. The nondimensional time used is $t^* U_f/C$ and the Reynolds number is given by $U_f C/\nu$. Re_t is the inverse of the subgrid eddy viscosity, which is modeled as

$$\frac{1}{Re_t} = C_s^2(\sqrt{g})^{2/3}|\mathbf{S}| \tag{4}$$

where $|\mathbf{S}|$ is the magnitude of the strain rate tensor given by $|\mathbf{S}| = \sqrt{2\bar{S}_{ik}\bar{S}_{ik}}$, and the Smagorinsky constant C_s^2 is obtained via the dynamic subgrid stress model (Germano et al. [28]).

The equations are formulated in a finite volume framework using a fractional-step algorithm for time advancement. Second-order central difference is used for the convective and viscous terms, and implicit Crank–Nicolson discretization is used for time advancement. During the start of each time step, the wing is moved based on the prescribed kinematics, keeping the external boundaries of the computational domain fixed. The resulting grid movement is carried out at each time step by a combination of a spring analogy and transfinite interpolations on displacements [29]. The space conservation law (1) is used to calculate the grid contravariant fluxes [29] that are used in the momentum equations to account for grid movement.

III. Results

The unsteady aerodynamics of flapping flight depends on many kinematic and flow parameters such as angle of attack, rotation and flapping kinematics, stroke amplitude, stroke plane angle, Reynolds number, and advance ratio. The purpose of the present study is to evaluate the effect of timing and duration of rotation and angle of attack on the force production for forward flights. All of the simulations in the current study are carried out at $Re = 10,000$ at an advance ratio $J = 0.5$. A stroke amplitude of 60 deg (± 30 deg) and a vertical stroke plane $\beta = 90$ deg are used. Three different rotational kinematics (delayed, symmetrical, and advanced) are analyzed to evaluate the effect of timing of rotation. The effect of duration of rotation is analyzed for symmetrical rotation with three different durations. Finally, the angle of attack during downstroke and upstroke are changed to analyze their effect on force production and the stability of the LEV.

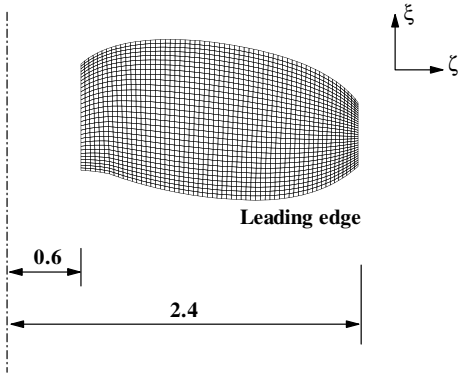

Fig. 2 Wing planform.

A. Comparison with Experiment

The dynamic mesh capability of the solver has been validated previously in a number of flow problems such as the forced oscillation of a cylinder, a pitching airfoil, and a hovering fruit fly [29,30]. In the current context, analysis of the hovering flight of a fruit fly with kinematics similar to that employed by Sane and Dickinson [22] is presented. The planform of the Robofly wing, as shown in Fig. 2 (obtained from Dickinson [21]), is used to develop the grid. The coordinates x, y, and z are used for the fixed frame, where the y–z plane represents the stroke plane (Fig. 1). The coordinates ξ, η, and ζ are used for the moving frame fixed to the wing, where ξ is along the chordwise direction, η is perpendicular to the wing, and ζ is along the spanwise direction (Fig. 2). The computational domain is made of 60 blocks with about 3 million cells. The domain boundaries are placed at 10 times the chord length from the edges of the wing on all sides except the symmetry surface, which is located at 0.6 times the chord length from the wing base (Fig. 2). The symmetric boundary condition is applied along the axis of flapping, and a zero-velocity boundary condition is applied at all other faces.

The simulation is carried out for four flapping cycles using 60 processors on System-X at Virginia Polytechnic Institute and State University. Comparison of lift and thrust forces between the third and fourth flapping cycles confirmed that the flow had attained repeatability, and hence the results from the fourth flapping cycle are used for the analysis. A triangular wave form for the flapping angle and a square wave form for the rotation angle, as shown in Fig. 3, are employed. The normalized values of $t^* = t/t_{\text{cycle}}$ from 0 to 0.5 represent the downstroke and from 0.5 to 1.0 represent the upstroke. The midstroke angle of attack is 50 deg for both strokes, and the rotation is carried out symmetrically with a total duration t^* of 0.16. The stroke plane angle is $\beta = 0$ deg, and the total flapping amplitude is $\Phi = 60$ deg. A fluid viscosity of 120 cSt with density of 880 kg/m^3 and flapping frequency of 168 mHz along with the actual length of the Robofly wing [22] (25 cm) are used to compute the Reynolds number for the current simulation. The Reynolds number based on the maximum chord length ($C = 10$ cm) and tip velocity is 73.

The comparison of time variation of lift and thrust forces obtained during the fourth flapping cycle with experimental results [22] is shown in Fig. 4. Because the stroke plane is horizontal ($\beta = 0$ deg), the lift force is given by $-F_x$ and the thrust force is given by $-F_y$. The lift force compares reasonably well; in particular, good agreement is observed during the upstroke, whereas the values differ during the downstroke. Because the kinematics are symmetrical and the freestream velocity is zero, the values of lift should be identical for the upstroke and downstroke. The comparison of thrust force also shows reasonable agreement in the trend, but the values differ in magnitude. In particular, the peak values of lift and thrust obtained at

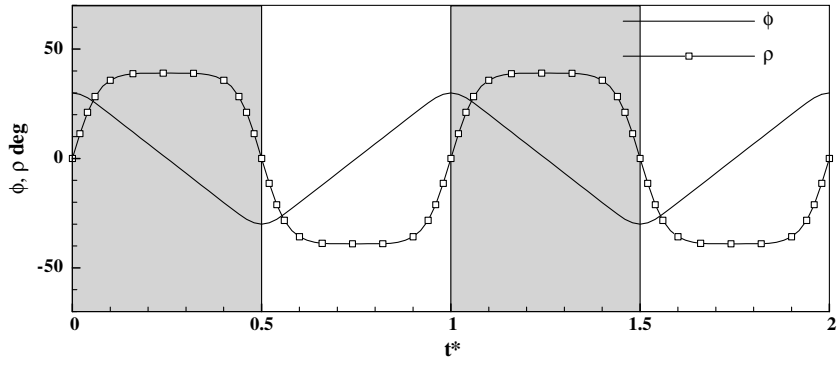

Fig. 3 Kinematics for hovering flight (shaded region represents downstroke).

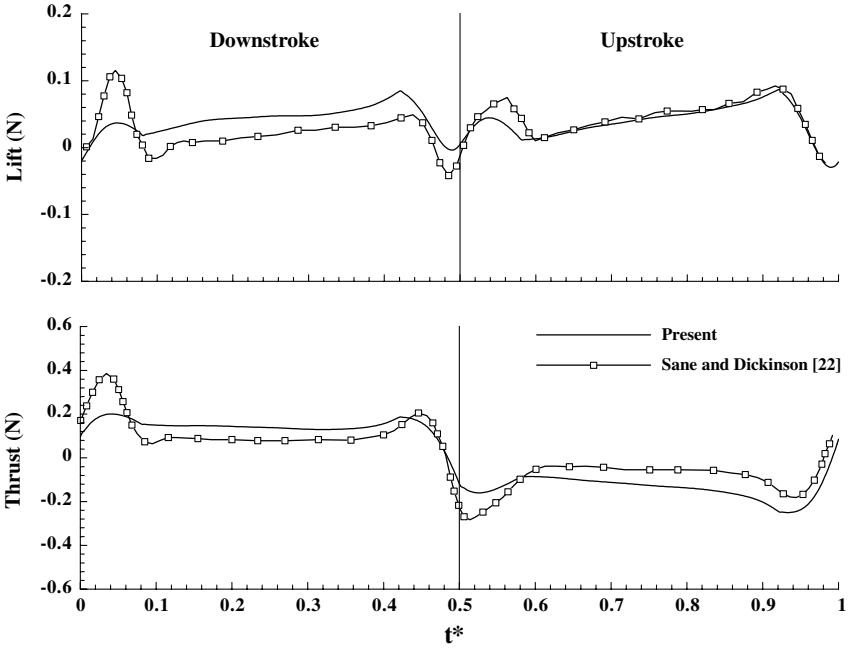

Fig. 4 Variation of lift and thrust forces for a hovering fruit fly.

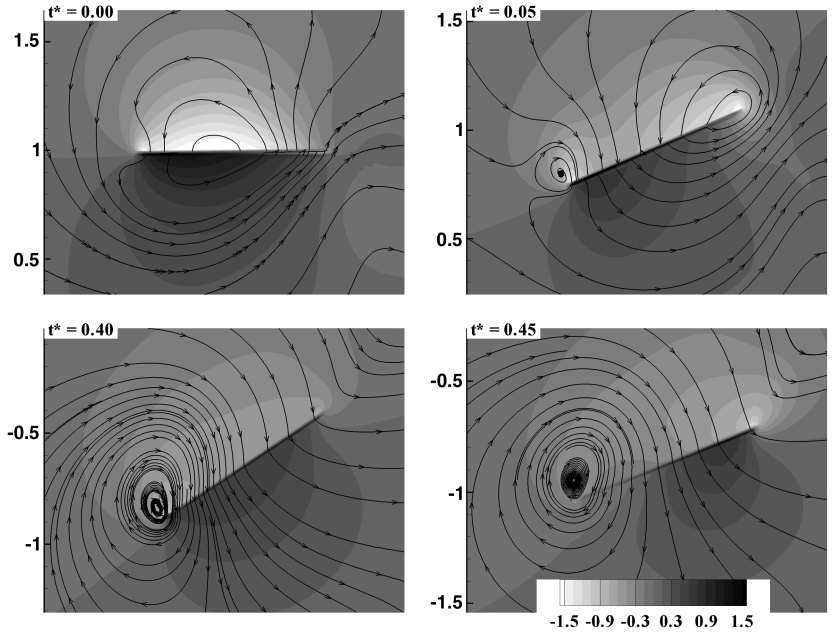

Fig. 5 Pressure contours and streamlines along the chordwise plane at $\zeta = 2$.

the start of the downstroke and upstroke show larger deviation from the experimental values. This deviation could be due to the kinematics used in the computations, which is curve-fitted from the experimental data, and results in some smoothing during stroke reversal. A previous study [17] has shown that the acceleration and deceleration during stroke reversal is responsible for the peaks in lift and thrust. Hence, a small deviation from the experimental kinematics could result in a larger deviation in the forces. Similar quantitative deviations have been reported by previous numerical studies [23,24,31]. Because the kinematics employed by the current study differs from these previous studies [23,24,31], direct comparison with their results is not made.

The pressure contours and streamlines in a chordwise plane at $\xi = 2$ at different times are shown in Fig. 5. Because the downstroke and upstroke are symmetric, only the results during the downstroke are used to analyze the flow structure. During the start of the downstroke, a high-pressure region forms on the bottom surface of

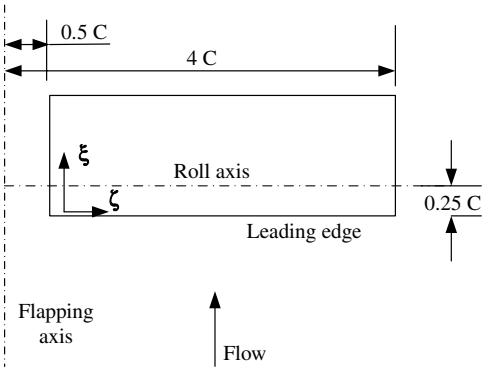

Fig. 6 Rectangular wing configuration.

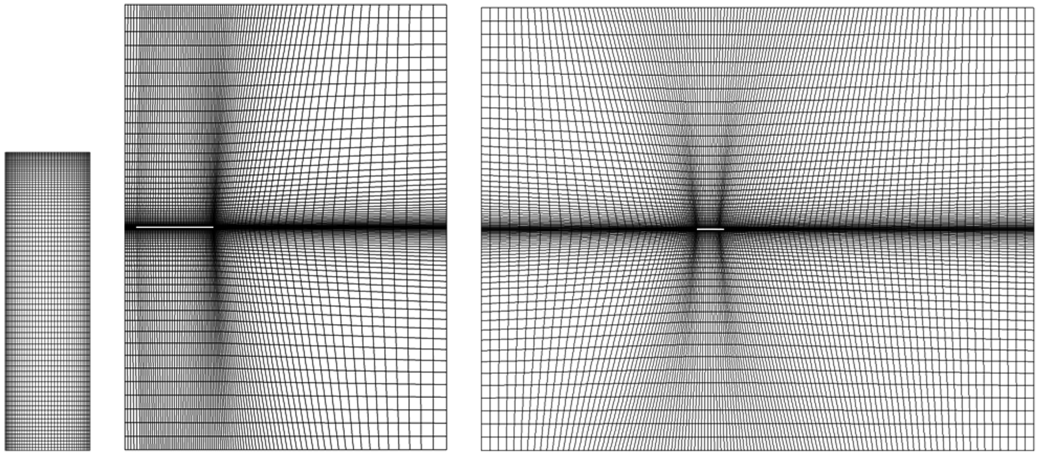

Fig. 7 Grid distribution: a) wing, b) spanwise plane (every other grid line is shown), and c) chordwise plane (every other grid line is shown).

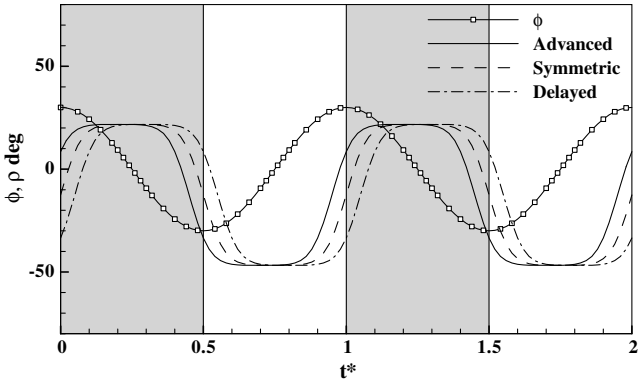

Fig. 8 Kinematics employed for cases A, B, and C (shaded region represents downstroke).

the wing due to the sudden deceleration of the wing at the end of the upstroke, which when combined with the rotation results in the formation of a LEV and a peak in lift and thrust at time $t^* = 0.05$. The LEV grows and reaches a maximum size at time $t^* \sim 0.4$ to 0.45 and sheds during the rotation, which reduces the lift and thrust production. At time t^* of 0.5 (not shown), the pressure contours are similar to that of $t^* = 0$, with the positive pressure now on the top surface of the wing.

B. Analysis of Forward Flight

For simplicity, an infinitesimally thin rectangular rigid wing with an aspect ratio of 4, as shown in Fig. 6, is used for the analysis. A single wing configuration with a symmetry boundary condition along the flapping axis is employed in the current study, assuming that there is no interference between wings and between fuselage and wing. The rotation axis is placed at the quarter-chord length from the leading edge. The downstream boundary is placed at 15 chord lengths from the trailing edge, and 10 chord lengths are used for other boundaries. Constant velocity boundary condition is applied at all inlet faces, and an outflow boundary condition is specified downstream. A symmetry condition is applied at the base of the wing. The grid consists of 60 blocks with approximately 8 million cells. The wing is resolved using 80×40 grid points, and 80 grid points are used perpendicularly to the wing, as shown in Fig. 7. The boundary layer is resolved by placing 10 grid points inside the thickness of 0.055, the typical boundary layer thickness for flow over a flat plate at $Re = 10,000$. A grid refinement study is carried out by increasing the number of grid points perpendicular to the wing from 80 to 120. The comparison of instantaneous lift and thrust forces shows less than 2% deviation, and the mean values of lift and thrust differ by less than 5%.

The kinematics involve a simple cosine wave form (Fig. 8) for flapping. The stroke plane angle is kept at $\beta = 90$ deg (vertical direction), and the total flapping amplitude is $\Phi = 60$ deg. The variations of kinematic parameters for the cases simulated in this study are given in Table. 2. Different rotation kinematics (Fig. 8) [namely, advanced, symmetric, and delayed rotation (cases A, B, and C) for duration $t^* = 0.1$] are used to study the effect of timing of rotation. To evaluate the effect of duration of rotation, simulations with a small time duration $t^* = 0.05$ (case D) and a larger duration (sinusoidal rotation, case E) are carried out. Additional simulations (cases F and G) with different angles of attack for both upstroke and downstroke are analyzed to evaluate the effect of angle of attack. For most cases, the angles of attack of 70 and 45 deg are used for the downstroke and upstroke, respectively. A lower value of angle of attack during the upstroke is used to reduce the downforce. The effective angle of attack α_{eff} is affected by both flapping velocity and freestream velocity, as shown in Fig. 9. In addition, due to the variation of flapping velocity U_f, the effective angle of attack varies along the span, with a maximum value at the tip. For the advance ratio of 0.5 and α_d of 70, the α_{eff} varies from -30 to 33 deg from base to tip. During the upstroke for α_u of 45, the value of α_{eff} varies from 45 to -18 deg.

C. Flow Structure and Lift and Thrust Variation

The critical flow structures obtained for forward flight for case B are discussed in this section. The simulations are carried out for four flapping cycles. The comparison of thrust and lift values between the third and fourth flapping cycles shows no deviation, Hence, the results from the fourth flapping cycle are used for the analysis.

1. During Downstroke

The sinusoidal variation of flapping angle results in acceleration during the first half of the downstroke and deceleration during the second half of the downstroke. The maximum flapping velocity occurs at $t^* = 0.25$, which results in a high effective angle of attack (Fig. 9). The isosurface of the ζ component of vorticity, given at

Table 2 Kinematic parameters used for different cases

Case	Rotation timing	Rotation duration	α_d	α_u
A	Advanced	0.1	70 deg	45 deg
B	Symmetric	0.1	70 deg	45 deg
C	Delayed	0.1	70 deg	45 deg
D	Symmetric	0.05	70 deg	45 deg
E	Sine wave	0.5	70 deg	45 deg
F	Sine wave	0.5	60 deg	35 deg
G	Sine wave	0.5	80 deg	55 deg

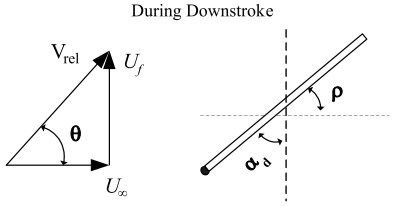

Fig. 9 Effective angle of attack during downstroke.

different times in Fig. 10, shows the formation of the LEV (negative vorticity) and its subsequent separation during the downstroke. At $t^* = 0.1$, the LEV forms near the tip and it is attached on the top surface of the wing. The LEV does not extend up to the base, as the effective angle of attack near the base is negative. At $t^* = 0.2$, a strong spiral LEV with a maximum size near the tip is formed, which results in a peak in lift (Fig. 11). The vorticity contours and the pressure contours at different spanwise locations at time $t^* = 0.25$ are shown in Fig. 12. The size of the LEV increases from base to tip. Strong positive vorticity is present between the LEV and the wing due to the induced velocity field, and the strength of the positive vorticity also increases along the spanwise direction. In addition, the separation of the LEV results in the formation of a second LEV. The second LEV also lifts away from the surface of the wing. The pressure contours show the detachment of the LEV (low-pressure region) and subsequent increase in the pressure on the surface of the wing by the entrainment of fluid from the freestream.

To analyze the structure of the LEV, particle traces are obtained by releasing particles along the leading edge. The particle traces at $t^* = 0.25$ (Fig. 13a) show a spiral LEV attached near the base and lifted from the wing near the tip. The contours of the ζ component of velocity, along the center of the LEV (Fig. 13b) show a strong spanwise velocity of the order of flapping velocity from the base to the tip. Similar results were obtained by the flow-visualization studies conducted by Ellington [9] using a large mechanical model of a hawk moth at ($Re \sim 4000$). They showed a spiral LEV with spanwise velocities comparable with the flapping velocity during the downstroke and also suggested that the spanwise flow removed the vorticity from the LEV and stabilized it. However, the present results show that the spanwise flow does not stabilize the LEV for forward flight. The chief reason is the presence of strong negative spanwise velocity near the tip, shown by the curved arrow (Fig. 13b), which prevents the removal of vorticity from the LEV. Hence, the vorticity starts building up near the tip, due to both the high angle of attack and the convection of vorticity from the base. This increase in vorticity leads to an instability in the LEV and consequent separation from the wing. The isosurface of vorticity at time $t^* = 0.4$ shows the complete separation of the LEV near the tip (Fig. 10), which results in a low lift coefficient. The isosurface also shows the presence of small negative vorticity due to secondary-vortex formation along the leading edge.

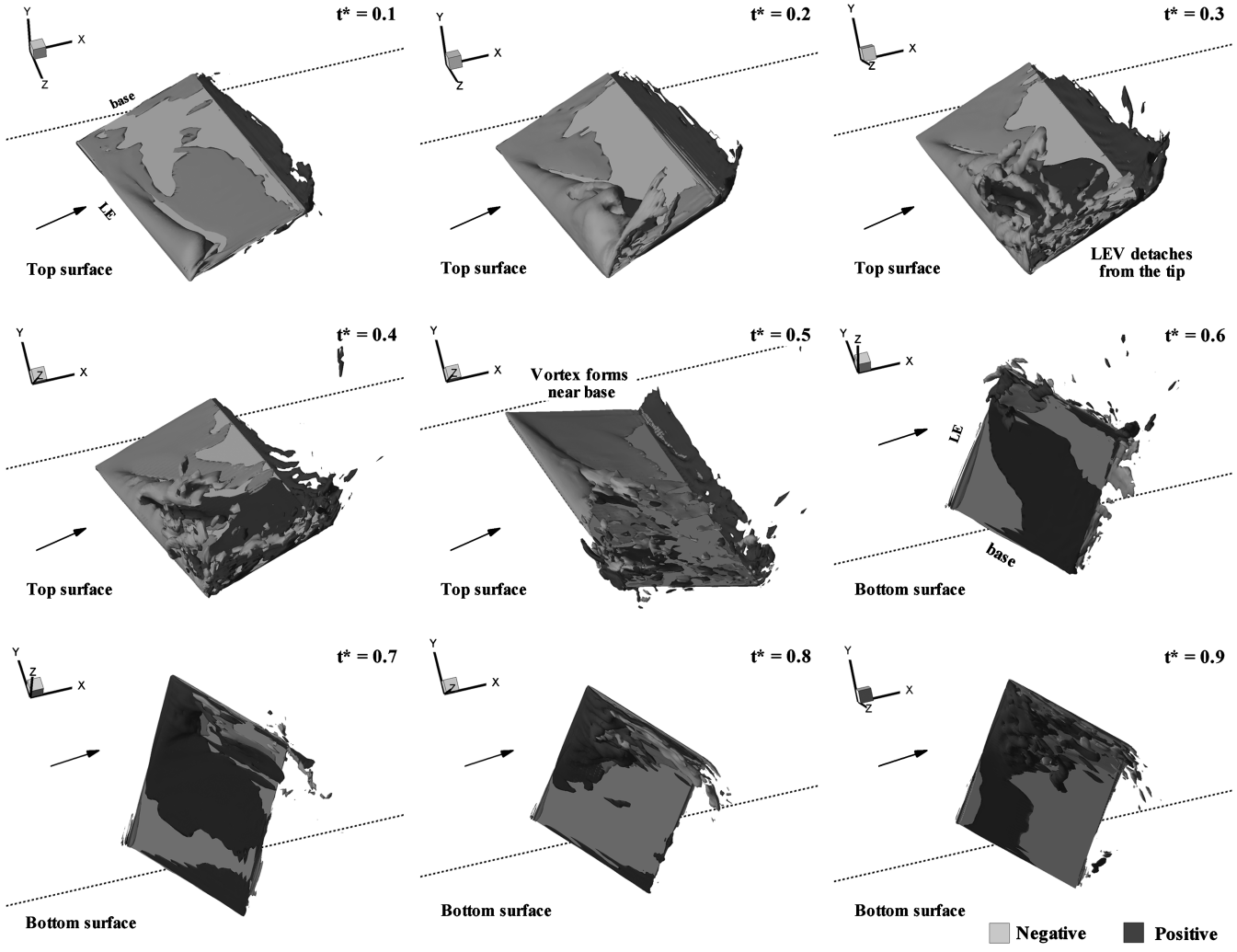

Fig. 10 Isosurface of ζ component of vorticity at different times (arrows represent approximate freestream direction and the dotted line represents the axis of flapping).

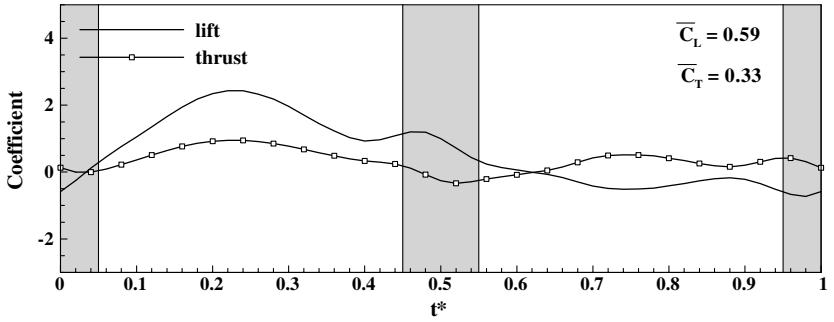

Fig. 11 Variation of lift and thrust coefficients (shaded region represents rotation).

2. During Supination

The supination starts at the end of the downstroke at around 0.45 and is carried out until $t^* = 0.55$, the start of the upstroke. The isosurface contours at time t^* of 0.4 (Fig. 10) show that the LEV is still attached at around $\zeta = 1$, with no LEV formation near the base. The increase in angle of attack during supination results in the formation of a vortex near the base, which extends the LEV from the middle to the base, as shown by the isosurface of vorticity at t^* of 0.5 (Fig. 10). This results in a second peak in lift. However, due to the rotation, the contribution of the LEV to thrust drops continuously (Fig. 11) and results in drag during the later part of supination.

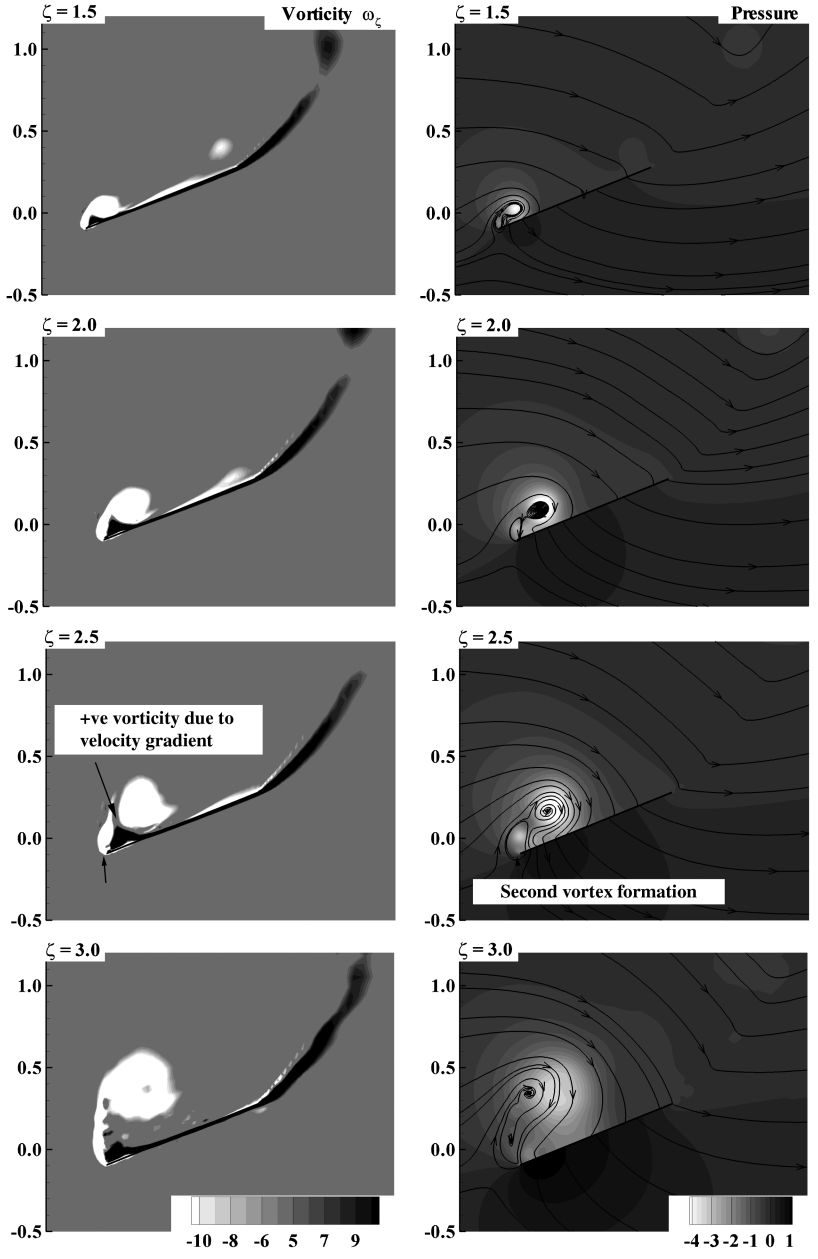

Fig. 12 Vorticity and pressure contours at various spanwise locations for time $t^* = 0.25$.

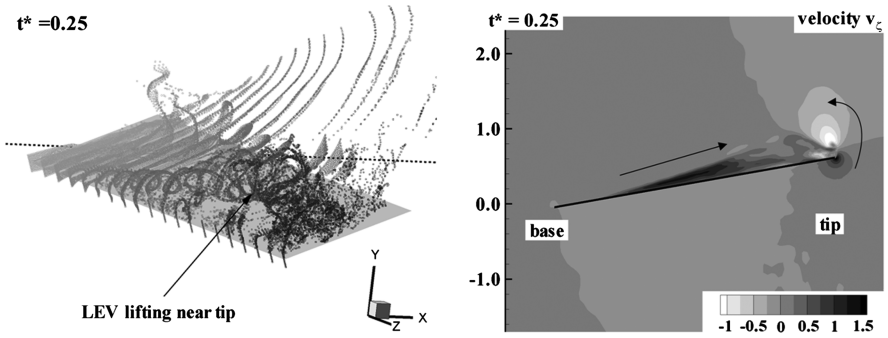

Fig. 13 Structure of LEV a) particle traces obtained by releasing particles along the leading edge (shaded based on the location of release) and b) spanwise flow along the center of the LEV (arrows indicate the direction of flow).

3. During Upstroke

The behavior of flow during the upstroke is similar to that during the downstroke. During the upstroke, the effective angle of attack is low and it is negative only for a small portion of the wing near the tip. Hence, there is no clear formation of the LEV, and the vorticity contours at time $t^* = 0.7$ (Fig. 10) show a small positive vortex attached near the tip. The vorticity and pressure contours at t^* of 0.75 (Fig. 14) show no apparent vortex formation at locations $\zeta = 1.5$ and

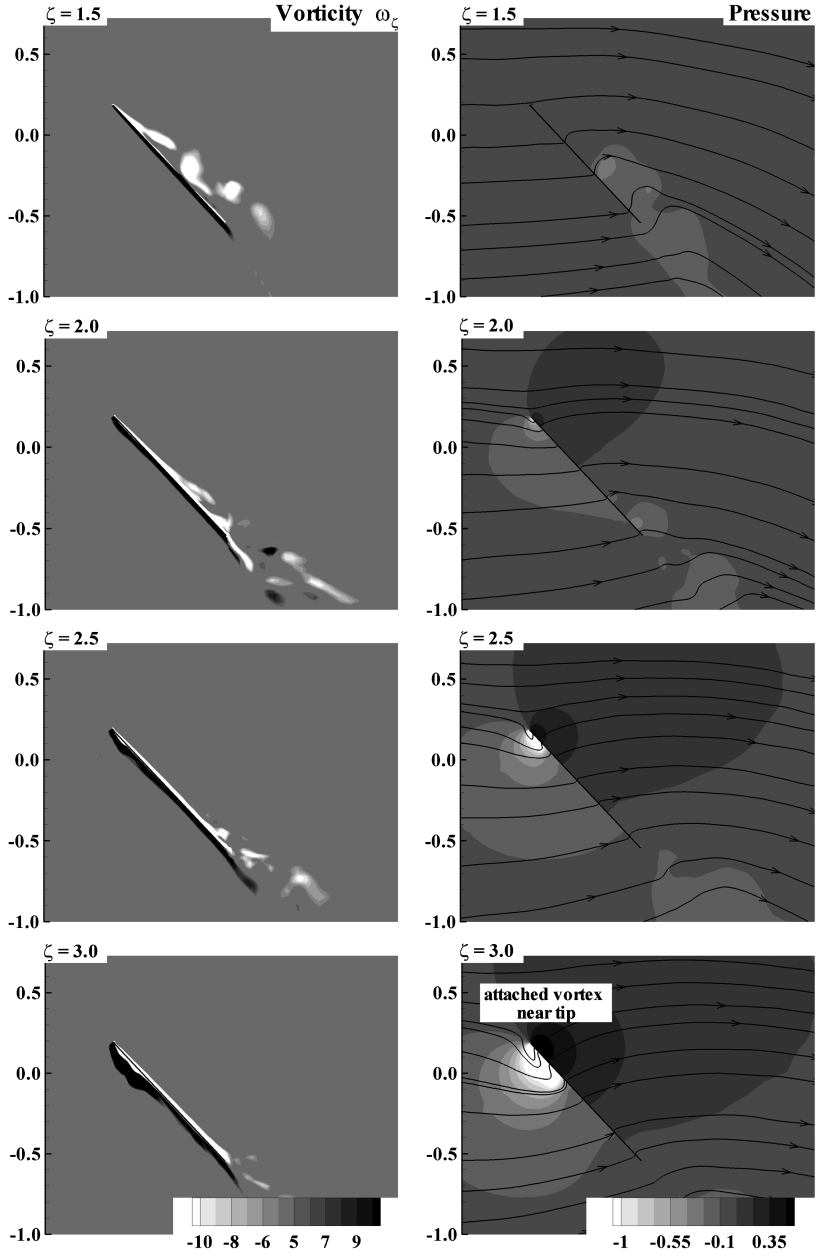

Fig. 14 Vorticity and pressure contours at various spanwise location for time $t^* = 0.75$.

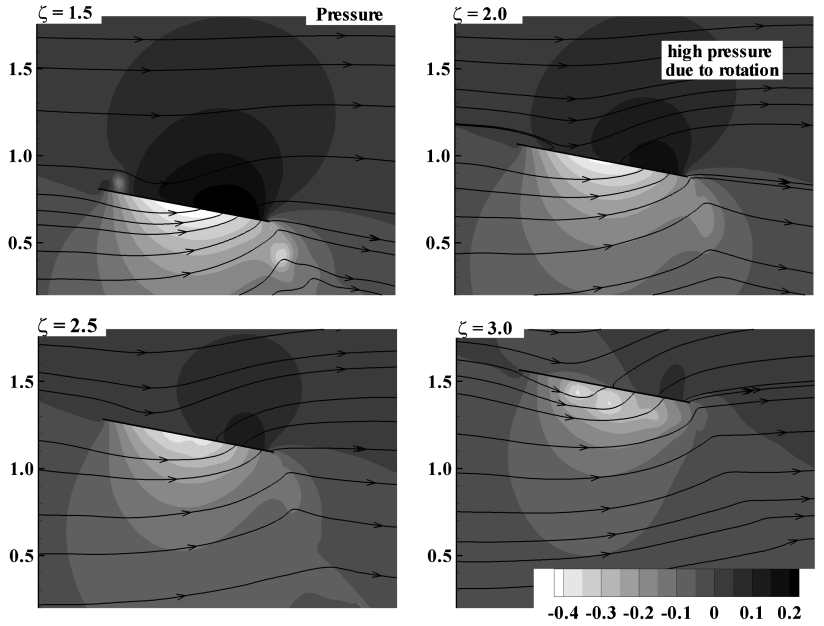

Fig. 15 Pressure at various spanwise location for time $t^* = 1.0$.

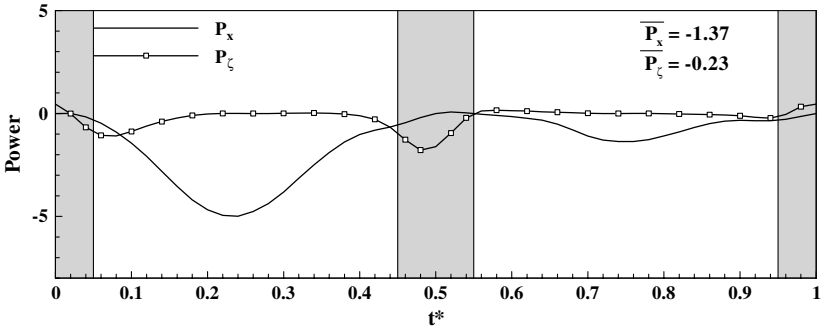

Fig. 16 Power required for rotation and flapping.

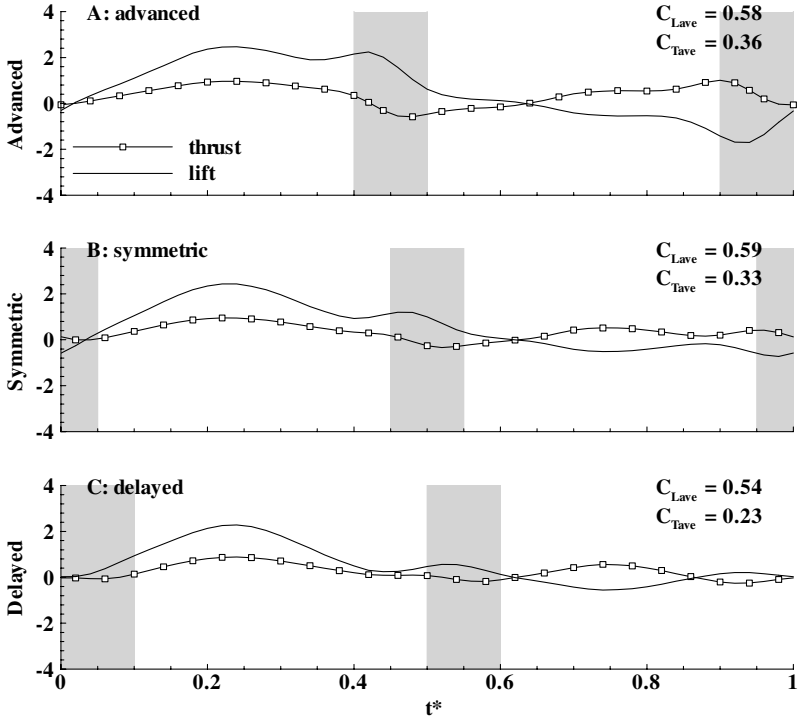

Fig. 17 Variation of lift and thrust for three different rotation timings (shaded region represents rotation).

2.0. A small vortex forms near the tip, which results in a low-pressure region on the bottom surface of the wing at locations $\zeta = 2.5$ and 3.0. This low-pressure region results in a peak in negative lift and also generates thrust. The vortex formed is attached to the wing and there is no secondary-vortex formation as observed during the downstroke. The vortex becomes unstable at around t^* of 0.8, as shown in Fig. 10, with a drop in negative lift.

4. *During Pronation*

During pronation the angle of attack near the base becomes negative. This change in angle of attack does not result in the formation of a LEV near the base as observed during supination. This is probably due to the absence of a strong LEV during the upstroke. However, a strong pressure difference across the surface is established at time $t^* = 1.0$ near the base, as shown in Fig. 15 at locations $\zeta = 1.5$ and 2.0. Because the axis of rotation is at the quarter-chord length from the leading edge, the trailing edge undergoes significant rotation, which results in strong positive pressure on the top near the trailing edge. However, the pressure difference at locations $\zeta = 2.5$ and 3.0 is not significant, due to the presence of separated vortex (Fig. 10, $t^* = 0.9$). A second peak in the downforce occurs that results in thrust during early periods of pronation.

5. *Lift and Thrust Production*

Instantaneous variations of lift and thrust coefficients (normalized based on the flapping velocity and planform area) are shown in Fig. 11. During the first half of the downstroke, the lift increases due to the formation of the LEV and reaches a maximum value of 2.5 at time 0.2. This value is around three times higher than the maximum coefficient of lift, 0.75, of a two-dimensional thin plate under steady-state condition. The thrust production is positive during most of the downstroke, except during rotation at the end of the downstroke. The contribution from pressure forces is dominant, and the torsional angle determines the ratio of thrust-to-lift force produced by the LEV. During the upstroke, a low-pressure region forms on the bottom surface, leading to a negative lift force, but the magnitude is less than that during the downstroke, due to the lower angle of attack. The thrust production is positive during most of the upstroke, with two peaks obtained at $t^* = 0.75$ and 0.95. The average coefficients of lift and thrust are 0.59 and 0.33, respectively. For a typical semiwingspan $R = 7.5$ cm, the lift produced can support 394 g and the thrust force generated is 1.08 N.

6. *Power Requirement and Propulsive Efficiency*

The power requirements for flapping (P_x) and rotation (P_ζ) are computed based on the torque generated by the fluid forces and angular velocity of the wing:

$$T = \int r \times (p + \tau)\, \mathrm{d}s; \qquad P = T \cdot \Omega \tag{5}$$

where r is the radius from the axis, p is the pressure, τ is the shear stress, and Ω is the angular velocity of the wing. The power required for acceleration of the wing is neglected, as the typical mass of membrane flapping wings is small. The instantaneous variation of power requirement (normalized based on fluid density, tip velocity, and chord length $\rho U_f^3 C^2$) shown in Fig. 16 follows a similar trend to that of lift and thrust. A peak in power requirement for flapping of around 5 occurs at $t^* = 0.2$ during the downstroke, which corresponds to the formation of the LEV. The power required during the upstroke is much lower than that during the downstroke, due to lower force production. The power requirement for rotation reaches a maximum value of 2 during the middle of rotation. The average power required for flapping and rotation are 1.37 and 0.23, respectively, and the propulsive efficiency [Eq. (6)] is 19.59%. The present simulation shows that flapping flight is capable of supporting the weight of MAVs and produces a propulsive thrust force:

$$\eta_{\text{prop}} = \frac{F_T U_\infty}{P} \tag{6}$$

D. Effect of Rotation Timing

The rotation at the end of translation changes the angle of attack and introduces vorticity ω_ζ of magnitude twice that of its angular velocity Ω_ζ. The lift and thrust variations for three different rotation kinematics (cases A, B, and C) are shown in Fig. 17. Figure 18 shows the isosurface of vorticity ω_ζ for all rotation timings during the middle of supination. During supination (rotation at the end of downstroke), the change in angle of attack and the introduction of negative vorticity extends the LEV from the middle of the wing to the base, which results in a second peak in lift. The strength of the vortex formed and the magnitude of lift depend on the timing of rotation (in other words, on the flapping velocity), which affects the effective angle of attack. A stronger vortex near the base for advanced rotation

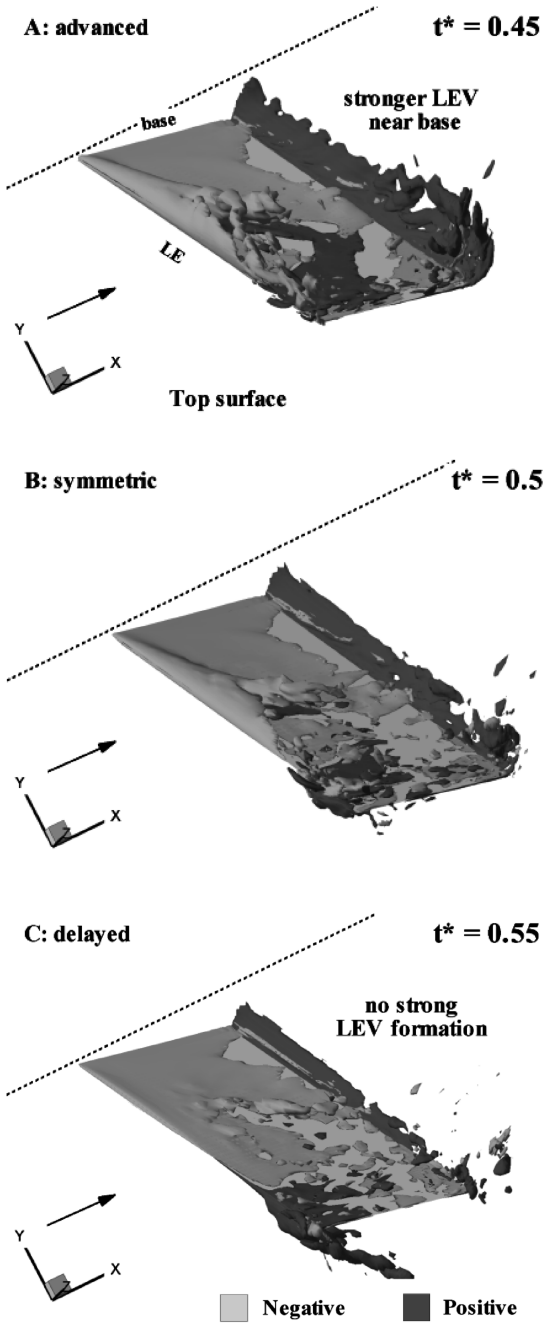

Fig. 18 Isosurface of the ζ component of vorticity during the middle of supination for different rotation timings.

Table 3 Average value of lift and thrust, and propulsive efficiency

Cases	C_T	C_T	Power flapping	Power rotation	Propulsive efficiency
A	0.58	0.36	1.65	0.32	17.36
B	0.59	0.33	1.37	0.23	19.59
C	0.54	0.23	1.18	0.17	16.19
D	0.59	0.33	1.37	0.25	19.35
E	0.52	0.37	1.59	0.21	19.53
F	0.57	0.28	1.17	0.36	17.39
G	0.45	0.30	1.98	0.08	13.83

and a smaller vortex for symmetric rotation are observed, as shown in Fig. 18. For delayed rotation, the vortex formation is insignificant. In the case of advanced rotation, the flapping velocity (Fig. 9) is in the positive direction, which enhances the change in angle of attack and hence results in a stronger vortex and high lift. On the other hand, in delayed rotation, the flapping velocity is in the opposite (down) direction, which counteracts the change in angle of attack, resulting in no vortex formation and a small peak in lift. A similar variation in lift occurs during pronation at the end of the upstroke.

The thrust production during upstroke and downstroke is high for advanced rotation, as it facilitates the formation of the LEV earlier,

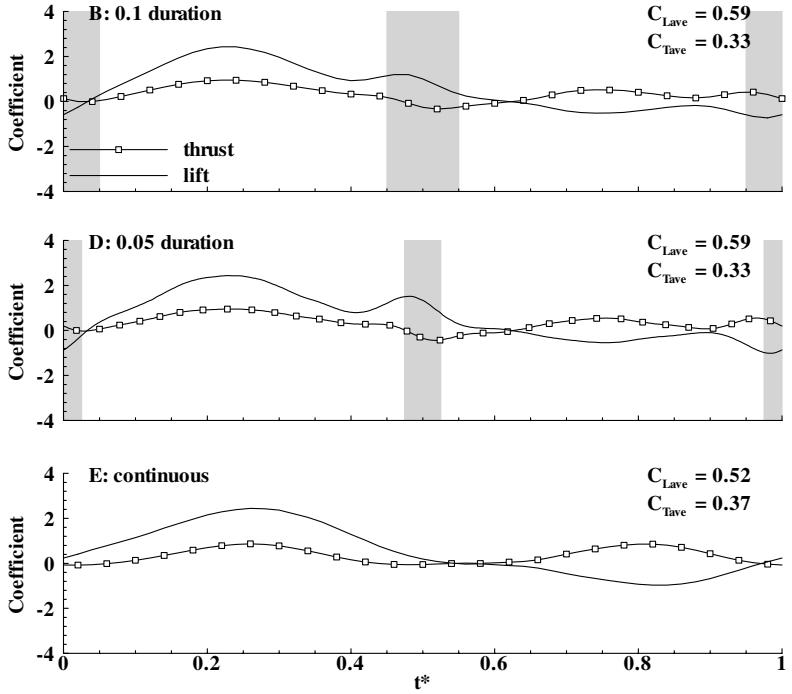

Fig. 19 Variation of lift and thrust for different rotation durations.

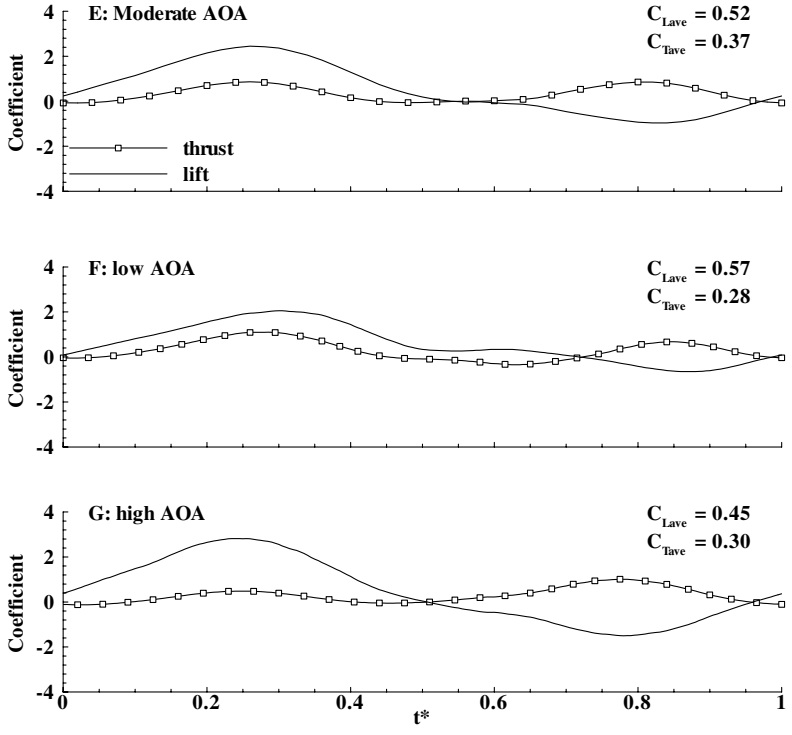

Fig. 20 Variation of lift and thrust for different angles of attack (AOA).

which results in high average values of thrust (Table 3). The delayed rotation results in lower thrust ($C_{T\text{avg}} = 0.23$), as it affects thrust production during translation and also results in significant drag during both supination and pronation. The symmetric rotation produces slightly lower thrust and higher lift than advanced rotation. However, symmetric rotation has better propulsive efficiency, due to the lower power requirement for flapping and rotation. Delayed rotation has low propulsive efficiency, which is undesirable for steady flight. Despite the differences in propulsive efficiency, different combinations of rotation timing could be used to achieve a required force. For example, to maximize lift production, advanced rotation for the downstroke and delayed rotation for the upstroke are preferable.

E. Effect of Duration of Rotation

To understand the effect of duration of rotation, a short rotation $t^* = 0.05$ (case D) and a continuous sinusoidal rotation (case E) are analyzed. The comparison of lift and thrust variation for cases B, D, and E is shown in Fig. 19. The peak in lift obtained for the short duration is higher than that observed for case B, which is mainly due to the higher angular velocity. On the other hand, continuous rotation does not produce any separate peaks in lift, instead delaying the location of maximum peak in lift from a t^* of 0.23 to 0.27. In continuous rotation, the rotation introduces positive vorticity (reduces angle of attack) during the first half of the downstroke and introduces negative vorticity (increases angle of attack) during the second half of the downstroke. This change in angle of attack delays the formation of the LEV during the first half and enhances the vortex formation near the base during the second half. The variation of lift reflects this effect. A gradual increase in lift occurs until $t^* = 0.27$, and a gradual drop in lift occurs during the second half of downstroke.

For case D, because the instantaneous value of lift is high only for a short duration, the average values of lift and thrust values remain unaffected. The thrust produced by continuous rotation ($C_{T\text{ave}} = 0.37$) is higher than other cases, which is mainly due to positive thrust production throughout the flapping cycle. The propulsive efficiencies of all three cases are equal, which shows that any duration of rotation could be used to achieve a desired force requirement. Hence, to achieve a higher thrust, a continuous rotation is preferable, whereas for higher lift, a combination of shorter supination and longer pronation is preferable.

F. Effect of Angle of Attack

To analyze the effect of angle of attack on force production, additional simulations with higher and lower angles of attack than case E are carried out. The variation of lift and thrust for cases E to G are shown in Fig. 20. The resultant force is almost perpendicular to the wing direction during the entire flapping cycle, due to the strong contribution of pressure forces. The torsional angle/angle of attack determines the contribution of total force to thrust and lift. In the case of low angle of attack, the instantaneous thrust values are higher than

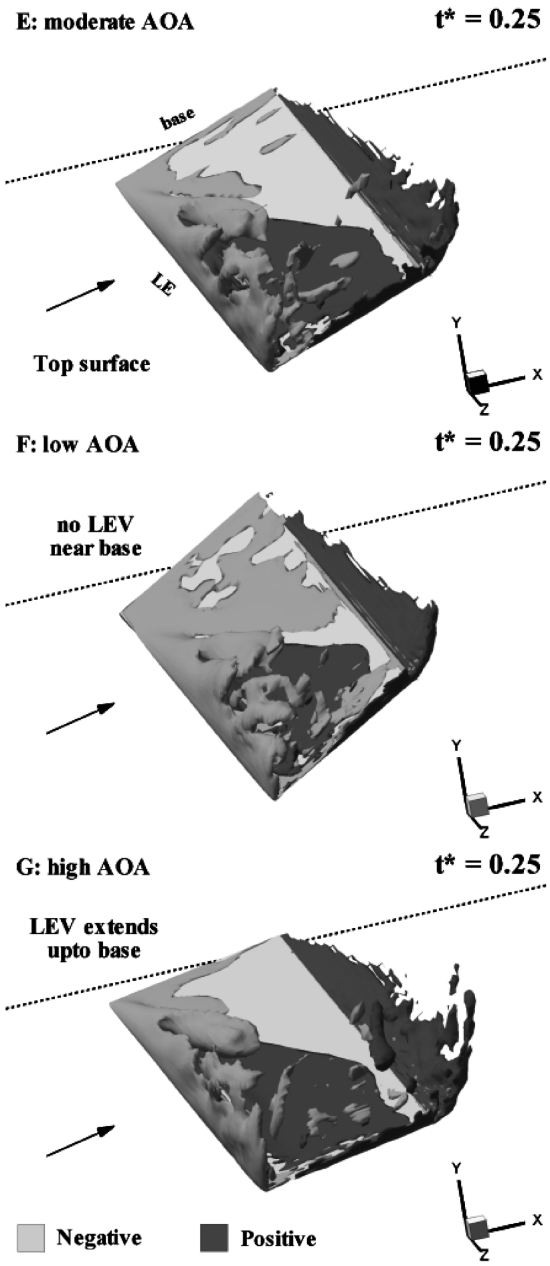

Fig. 21 Isosurface of vorticity during the middle of downstroke for different angles of attack.

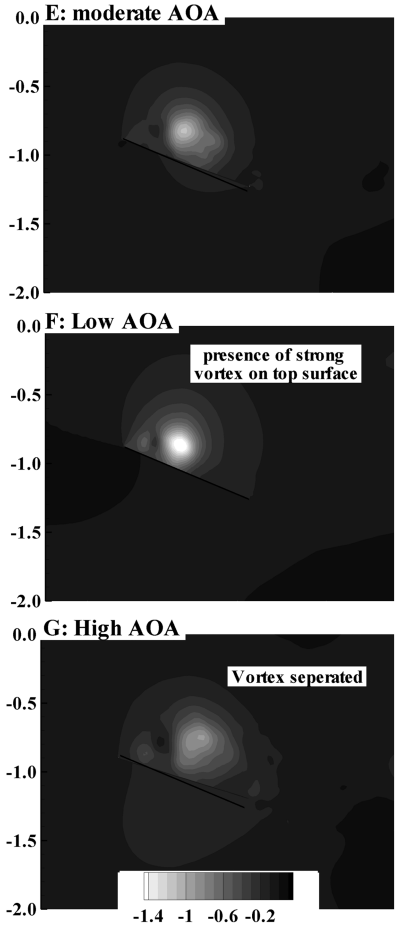

Fig. 22 Pressure contour at location $z = 2.0$ at time $t^* = 0.55$.

the other two cases and are of the same order as that of lift, whereas at a high angle of attack, the resultant force contributes mainly to lift. In addition, the location of maximum lift and the gradient of the lift profile changes for all three cases. The isosurface of vorticity for all three cases E–G during the middle of the downstroke is shown in Fig. 21. In the case of high angle of attack, the LEV extends up to the base at $t^* = 0.25$ and it separates completely from the wing during the second half of the downstroke. This results in sharp changes in lift and the maximum lift occurs early. In the case of low angle of attack, the LEV formation does not extend up to the base (Fig. 21) during the early stages of the downstroke. During the first half of the downstroke, the LEV formed near the tip contributes to lift, and the formation of the LEV near the base contributes to lift during the second half of downstroke. Hence, the variation of lift is gradual and the location of maximum lift shifts to $t^* = 0.35$.

The average value of thrust is high for the moderate-angle-of-attack case, whereas high lift is produced by the low-angle-of-attack case. The low angle of attack produces high instantaneous values of thrust during the downstroke. However, due to the incomplete separation of the LEV at the end of the downstroke, it results in considerable drag during the initial stages of the upstroke. Figure 22 shows the pressure contours at location $\zeta = 2.0$ at time $t^* = 0.55$ for all three angles of attack. A strong vortex and low-pressure region are present for the low angle of attack, whereas the strength of the vortex and the pressure difference across the surface are small for the other cases. The pressure difference in case of the low angle of attack results in high lift and drag until $t^* = 0.6$, which reduces the propulsive efficiency. The propulsive efficiency of case E is high, and the high angle of attack, case G, results in low propulsive efficiency. Hence, to achieve high thrust production, an optimum value of angle of attack that results in complete shedding of the LEV at the end of the downstroke is required. Further, if high lift force is required, a combination of high angle of attack during the downstroke and a low angle of attack during the upstroke could be used.

IV. Conclusions

The effect of rotation kinematics and angle of attack on forward flapping flight with an advance ratio of 0.5 is analyzed at a Reynolds number of 10,000. The flow structures obtained for all cases show the presence of a spiral leading-edge vortex (LEV) on the top surface during the downstroke. The LEV becomes unstable and separates during the middle of the downstroke despite the presence of spanwise flow along the core of the LEV. The negative spanwise flow created by the tip blocks the removal of vorticity from the LEV, which leads to the subsequent separation of the LEV near the tip, leading to a drop in force production. The separation of the LEV results in the formation of a secondary vortex. However, the secondary vortex is not attached to the wing, and hence no increase in lift is observed during the second half of the downstroke. The average lift force generated is enough to support the typical weight requirement of 100 to 200 g of micro air vehicles and generates thrust with a propulsive efficiency of 20%.

Analysis of various kinematics shows that the formation and separation of the LEV and the instantaneous variation of forces depend strongly on kinematics. Analysis of different rotation kinematics shows that a stronger LEV forms near the base during advanced rotation and when rotation occurs over a small time duration. This formation of a stronger LEV leads to higher force production during supination and pronation and subsequently affects the average values of lift and thrust. For continuous rotation kinematics, thrust is produced throughout the flapping cycle, resulting in high propulsive efficiency. Analysis of different angles of attack shows that the growth and stability of the LEV depends strongly on the angle of attack. For a low angle of attack, the LEV stays attached longer and generates higher thrust during the downstroke. However, the presence of the attached LEV affects thrust generation in the subsequent upstroke, leading to a drop in the average thrust. Finally, among all the cases analyzed, continuous rotation with a moderate angle of attack performs better in terms of propulsive efficiency and thrust. At the same time, different combinations of rotation and/or angle of attack could be employed to achieve the desired force requirements for different flight conditions.

References

[1] McMasters, J. H., and Henderson, M. L., "Low-Speed Single-Element Airfoil Synthesis," *Technical Soaring*, Vol. 2, Nos. 1–2, 1980, pp. 1–21. doi:10.1016/0160-791X(80)90017-2

[2] Carmichael, B. H., "Low Reynolds Number Airfoil Survey," Vol. 1, NASA CR 165803, Nov. 1981.

[3] Pelletier, A., and Mueller, T. J., "Low Reynolds Number Aerodynamics of Low-Aspect-Ratio, Thin/Flat/Cambered-Plate Wings," *Journal of Aircraft*, Vol. 37, No. 5, 2000, pp. 825–832. doi:10.2514/2.2676

[4] Weis-Fogh, T., "Quick Estimate of Flight Fitness in Hovering Animals, Including Novel Mechanisms for Lift Production," *Journal of Experimental Biology*, Vol. 59, 1973, pp. 169–230.

[5] Dickinson, M. H., and Götz, K. G., "Unsteady Aerodynamic Performance of Model Wings at Low Reynolds Numbers," *Journal of Experimental Biology*, Vol. 174, 1993, pp. 45–64.

[6] Ellington, C. P., Berg, C. V. D., Willmott, A. P., and Thomas, A. L. R., "Leading-Edge Vortices in Insect Flight," *Nature*, Vol. 384, No. 6610, 1996, pp. 626–630. doi:10.1038/384626a0

[7] Dickinson, M. H., Lehmann, F.-O., and Sane, S. P., "Wing Rotation and the Aerodynamic Basis of Insect Flight," *Science*, Vol. 284, No. 5422, 1999, pp. 1954–1960. doi:10.1126/science.284.5422.1954

[8] Wang, Z. J., Birch, J. M., and Dickinson, M. H., "Unsteady Forces and Flows in Low Reynolds Number Hovering Flight: Two-Dimensional Computations vs Robotic Wing Experiments," *Journal of Experimental Biology*, Vol. 207, No. 3, 2004, pp. 449–460. doi:10.1242/jeb.00739

[9] Ellington, C. P., "The Novel Aerodynamics of Insect Flight: Applications to Micro-Air Vehicles," *Journal of Experimental Biology*, Vol. 202, 1999, pp. 3439–3448.

[10] Liu, H., Ellington, C. P., Kawachi, K., Berg, C. V. D., and Willmott, A. P., "A Computational Fluid Dynamic Study of Hawkmoth Hovering," *Journal of Experimental Biology*, Vol. 201, 1998, pp. 461–477.

[11] Birch, J. M., and Dickinson, M. H., "Spanwise Flow and the Attachment of the Leading-Edge Vortex on Insect Wings," *Nature*, Vol. 412, No. 6848, Aug. 2001, pp. 729–733. doi:10.1038/35089071

[12] Birch, J. M., Dickson, W. B., and Dickinson, M. H., "Force Production and Flow Structure of the Leading Edge Vortex on Flapping Wings at High and Low Reynolds Numbers," *Journal of Experimental Biology*, Vol. 207, No. 7, 2004, pp. 1063–1072. doi:10.1242/jeb.00848

[13] Miller, L. A., and Peskin, C. S., "When Vortices Stick: An Aerodynamic Transition in Tiny Insect Flight," *Journal of Experimental Biology*, Vol. 207, 2004, pp. 3073–3088. doi:10.1242/jeb.01138

[14] Shyy, W., and Liu, H., "Flapping Wings and Aerodynamic Lift: The Role of Leading-Edge Vortices," *AIAA Journal*, Vol. 45, No. 12, 2007, pp. 2817–2819. doi:10.2514/1.33205

[15] Aono, H., Shyy, W., and Liu, H., "Vortex Dynamics in Near Wake of a Hovering Hawkmoth," 46th AIAA Aerospace Sciences Meeting and Exhibit, AIAA Paper 2008-583, Reno, NV, 2008.

[16] Mcclung, A., Maple, R., Kunz, D., and Beran, P., "Examining the Influence of Structural Flexibility on Flapping Wing Propulsion," 49th AIAA/ASME/ASCE/AHS/ASC Structures, Structural Dynamics, and Materials Conf., AIAA Paper 2008-1816, Schaumburg, IL, 2008.

[17] Ramamurti, R., and Sandberg, W. C., "A Computational Investigation of the Three-Dimensional Unsteady Aerodynamics of Drosophila Hovering and Maneuvering," *Journal of Experimental Biology*, Vol. 210, No. 5, 2007, pp. 881–896. doi:10.1242/jeb.02704

[18] Ramamurti, R., and Sandberg, W., "Computations of Insect and Fish Locomotion with Applications to Unconventional Unmanned Vehicles," *AIAA Journal*, Vol. 46, No. 9, 2008, pp. 2178–2190. doi:10.2514/1.32826

[19] Fry, S. N., Sayaman, R., and Dickinson, M. H., "The Aerodynamics of Free-Flight Maneuvers in Drosophila," *Science*, Vol. 300, No. 5618, 2003, pp. 495–498. doi:10.1126/science.1081944

[20] Tarascio, M. J., Ramasamy, M., Chopra, I., and Leishman, J. G., "Flow Visualization of Micro Air Vehicle Scaled Insect-Based Flapping

Wings," *Journal of Aircraft*, Vol. 42, No. 2, Apr. 2005, pp. 385–390. doi:10.2514/1.6055

[21] Dickinson, M. H., "The Effects of Wing Rotation on Unsteady Aerodynamic Performance at Low Reynolds Numbers," *Journal of Experimental Biology*, Vol. 192, 1994, pp. 179–206.

[22] Sane, S. P., and Dickinson, M. H., "The Control of Flight Force by a Flapping Wing: Lift and Drag Production," *Journal of Experimental Biology*, Vol. 204, 2001, pp. 2607–2626.

[23] Sun, M., and Tang, J., "Unsteady Aerodynamic Force Generation by a Model Fruit Fly Wing in Flapping Motion," *Journal of Experimental Biology*, Vol. 205, 2002, pp. 55–70.

[24] Ramamurti, R., and Sandberg, W., "A Three-Dimensional Computational Study of the Aerodynamic Mechanisms of Insect Flight," *Journal of Experimental Biology*, Vol. 205, May 2002, pp. 1507–1518.

[25] Thomas, A. L. R., Taylor, G. K., Srygley, R. B., Nudds, R. L., and Bomphrey, R. J., "Dragonfly Flight: Free-Flight and Tethered Flow Visualizations Reveal a Diverse Array of Unsteady Lift-Generating Mechanisms, Controlled Primarily Via Angle of Attack," *Journal of Experimental Biology*, Vol. 207, No. 24, 2004, pp. 4299–4323. doi:10.1242/jeb.01262

[26] Demirdzic, I., and Peric, M., "Space Conservation Law in Finite Volume Calculation of Fluid Flow," *International Journal for Numerical Methods in Fluids*, Vol. 8, No. 9, 1988, pp. 1037–1050. doi:10.1002/fld.1650080906

[27] Demirdzic, I., and Peric, M., "Finite Volume Method for Prediction of Fluid Flow in Arbitrarily Shaped Domains with Moving Boundaries," *International Journal for Numerical Methods in Fluids*, Vol. 10, No. 7, 1990, pp. 771–790. doi:10.1002/fld.1650100705

[28] Germano, M., Piomelli, U., Moin, P., and Cabot, W. H., "A Dynamic Subgridscale Eddy Viscosity Model," *Physics of Fluids A*, Vol. 3, 1991, pp. 1760–1765. doi:10.1063/1.857955

[29] Gopalakrishnan, P., and Tafti, D. K., "A Parallel Boundary Fitted Dynamic Mesh Solver for Applications to Flapping Flight," *Computers and Fluids*, Vol. 38, No. 8, Sept. 2009, pp. 1592–1607. doi:10.1016/j.compfluid.2009.01.006

[30] Gopalakrishnan, P., and Tafti, D. K., "A Parallel Multiblock Boundary Fitted Dynamic Mesh Solver for Simulating Flows with Complex Boundary Movement," AIAA 38th Fluid Dynamic Conf., AIAA Paper 2008-4142, Seattle, WA, June 2008.

[31] Sun, M., and Lan, S. L., "A Computational Study of the Aerodynamic Forces and Power Requirements of Dragonfly (Aeschna Juncea) Hovering," *Journal of Experimental Biology*, Vol. 207, 2004, pp. 1887–1901. doi:10.1242/jeb.00969

P. Beran
Associate Editor